



Utilizing a Cornu depolarizer in the generation of spatially unpolarized light

FLORIAN KROH, MARKUS ROSSKOPF, AND WOLFGANG ELSÄSSER* 

Institute of Applied Physics, Technische Universität Darmstadt, 64289 Darmstadt, Germany

*Corresponding author: elsaesser@physik.tu-darmstadt.de

Received 30 March 2021; revised 11 May 2021; accepted 11 May 2021; posted 12 May 2021 (Doc. ID 426517); published 1 June 2021

In this paper, we investigate depolarization properties of a quartz double-wedge Cornu depolarizer with respect to the generation of spatially unpolarized light in terms of on-average randomly occupied states on the Poincaré sphere. Spatially resolved Stokes parameter measurements yield transformed polarization states and polarization-dispersed characteristic fringes for the Stokes parameters. Their spatial symmetry, the degree of polarization, and spatially integrated Stokes parameters as a function of the aperture-determined input diameter together with a Mueller matrix calculus model confirm the successful generation of equator states incorporating the ensemble of all purely linearly polarized states, thus on spatial average representing unpolarized light. © 2021 Optical Society of America

<https://doi.org/10.1364/AO.426517>

1. INTRODUCTION

Polarization is a central and intriguing property of light with a broad impact in many areas of modern optics. In particular, unpolarized light in its many manifestations has recently experienced a renaissance of interest through a comprehensive overview on latent polarization of unpolarized light and its higher-order correlations by Goldberg *et al.* [1]. Originally the discovery of unpolarized light goes back to natural light [2,3] in the era of French optics pioneers [4,5]. Nowadays, in theory, unpolarized light is discerned by inspecting the invariance regarding its direction of propagation, handedness, or phase changes under the influence of wave-plates [6–9].

Recently, the intrinsic polarization structure of unpolarized light was investigated in the temporal domain by Setälä *et al.* who introduced the notion of an instantaneous polarization state [10], later demonstrated experimentally by Shevchenko *et al.* [11,12], leading to applications such as ghost polarization communication [13], ghost polarimetry, [14] and discrimination of types of unpolarized light via polarization correlation measurements [15].

Depolarization is a key concept for a multitude of applications such as fiber-optic communications [16,17], reducing polarization-dependent gain [18], quantum communications [19–21], polarization scrambling [22], oceanography [23], and even navigation [24]. Reducing polarization bias is also crucial for sensing instruments such as photomultipliers and grating spectrometers [25]. However, depolarizers also play an important role in exploring fundamental physics such as optical activity [26,27], generation of vector beams [28,29], and separating photon spins [30].

In the spatial domain, depolarization has been studied extensively for full Poincaré beams [31] or complex Poincaré beams in holography [32], for uni-axial crystals producing non-uniformly (totally) polarized beams [33,34] and for light scattered by compressed powders [35,36], and it has been exploited in designing depolarizers based on liquid crystals [37] and metasurfaces [38]. Commonly used double-wedge configurations such as the dual Babinet compensator and the Cornu depolarizer have been interpreted in theory by McGuire *et al.* [25], and in a more general context, the action of depolarizers via Mueller matrices is well investigated [39–41]. Numerical simulations exist for single-wedge depolarizers [42], Cornu depolarizers [43,44], and double-wedge depolarizers [42,45]. For the latter, longitudinal polarization periodicity of unpolarized light has been observed [46], and for polarized LED emission in combination with a digital micro-mirror device array, spatio-spectral coherence of depolarized light was probed [47]. Apart from examinations of optically active materials of Cornu depolarizers performed by Bagan *et al.* [48], a deeper insight and better understanding of the Cornu depolarizer's properties is still desirable. Our work aims to fill this gap.

Historically, one of the earliest tools for the depolarization of light is the Lyot depolarizer [5], which consists of two quartz plates with their fast axes separated by 45° and a plate thickness ratio of 2:1 [49], which is suited for broadband input light. Depolarization of light can also be achieved by temporally varying the rotation angles of two wave plates placed in series [49] and works for monochromatic light [50]. The Cornu depolarizer is another historically founded design based on two quartz wedges and related to the Cornu dispersion prism [51], both named in honor of Marie Alfred Cornu [52,53].

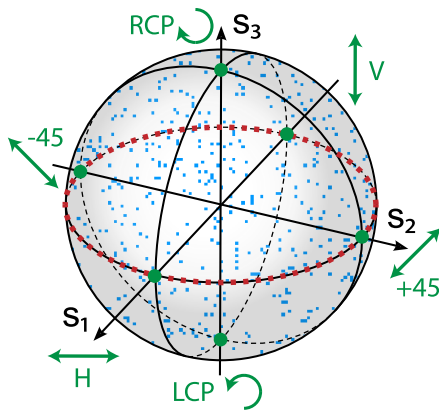


Fig. 1. Depiction of the Poincaré sphere, which is spanned by the three normalized Stokes vectors s_1 , s_2 , and s_3 . Shown are the well-defined states of fully polarized light (green dots) and selected examples of spatial polarization distributions of randomly polarized light as fully randomly covered Poincaré sphere (type I unpolarized light, indicated by blue dots) and fully encompassed equator states (indicated by red dots).

In our investigations, we focus on this type of depolarizer and characterize our Cornu depolarizer in the context of classical optics. Distinct linearly and circularly polarized input states of monochromatic helium–neon laser radiation with variable aperture-determined input diameter are transmitted through the Cornu depolarizer. Using a Schaefer–Collett [54] or Berry–Gabielse–Livingston polarimeter [55], the output polarization state of light transmitted by the Cornu depolarizer is analyzed by employing the Stokes parameter formalism [56] and Mueller matrix calculus. We record spatially resolved polarization distributions with a CCD camera and spatially integrated measurements using a photodetector. The obtained polarization states can be mapped on the Poincaré sphere [57] as depicted in Fig. 1 in the form of single Stokes vectors for fully polarized light [58] or as spatial distributions across the surface for unpolarized light [35,59].

Unpolarized light in this context means polarization of light encompassing not only a single point on the surface of the Poincaré sphere, but distinct areas. In analogy to temporally unpolarized light [11], spatially unpolarized light is considered fully polarized in one specific point in space whereas on spatial average, the light encompasses a superposition of many polarization states on the surface of the Poincaré sphere.

2. BASICS OF THE CORNU DEPOLARIZER

A double-wedge depolarizer made of an optically active material is also commonly known as a Cornu depolarizer. Our depolarizer consists of two identical prism wedges made of uniaxial, crystalline quartz that are optically cemented at their interface, as can be seen in Fig. 2. The optical axis of both wedges is oriented such that it is normal to the octagons' front facet. The circular birefringence of both wedges is slightly different with respect to left and right circularly polarized light, and the wedges have an opposite optical rotatory power [60]. For a monochromatic, linearly polarized, collimated plane-wave beam incident normal to the center of the Cornu depolarizer's front facet,

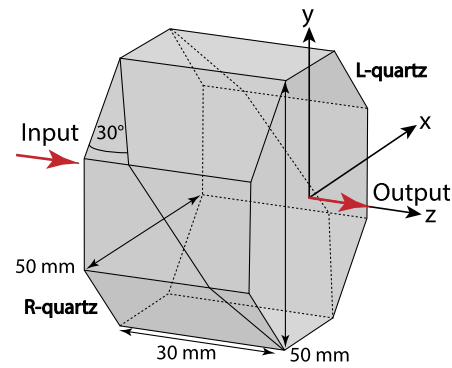


Fig. 2. Illustration of the Cornu depolarizer manufactured by B. Halle Nachf. GmbH. The depolarizer consists of two optically active quartz wedges cut at a wedge angle of 30°, joined at their interface, and oriented so that their optical axis is parallel to the impinging beam. Its dimensions are the following: clear aperture 50 mm, width 50 mm, and length 30 mm. Light enters the depolarizer from the left side and is transmitted through the right side of the octagon.

a rotation variation of the polarization axis induced by both wedges on the output light is given as follows [25]:

$$\phi = \rho_R L = \frac{2\pi}{\lambda} (n_l - n_r) L, \tag{1}$$

where L denotes the length of the Cornu depolarizer, λ the wavelength, and n_l and n_r are the indices of circular birefringence for left- and right-handed circularly polarized light, respectively. For quartz, the wavelength-dependent difference of the indices is $|n_l - n_r| = 6.6 \cdot 10^{-5}$ when illuminated with light from a helium–neon laser at 632.8 nm [60]. The term $\rho_R = \frac{2\pi}{\lambda} (n_l - n_r)$ represents the specific optical rotatory power of quartz. Minor effects such as scattering, absorption, refraction at the interface of the Cornu depolarizer, and temperature dependence of the rotatory power are neglected here. The Cornu depolarizer can be described within Mueller's formalism by the following matrix [25] using Eq. (1):

$$M_{\text{Cornu}} = \begin{pmatrix} 1 & 0 & 0 & 0 \\ 0 & \cos(\phi y) & \sin(\phi y) & 0 \\ 0 & -\sin(\phi y) & \cos(\phi y) & 0 \\ 0 & 0 & 0 & 1 \end{pmatrix}. \tag{2}$$

Here, y indicates the position on the exit pupil of the Cornu depolarizer as indicated in Fig. 2 and is normalized to ± 1 at the pupil's edge. The retardance $\Delta = \phi y + \gamma$ depends on the position y , where γ is the retardance at $y = 0$, and ϕ is its slope. The wedges of the Cornu depolarizer have the same slope value and zero offset with respect to each other. From this matrix, a mixing effect on linearly polarized components of input light is evident, since the four sine and cosine terms form a rotation matrix with respect to the s_1 and s_2 components of an input Stokes vector. The polarization axis of linearly polarized light is simply rotated about the spatially dependent angle ϕ , while circularly polarized input light is not affected by the Cornu depolarizer. In the following experimental setup as shown in Fig. 3, a circular iris aperture in front of the CD is used to select a desired aperture-determined input diameter of light impinging on the Cornu depolarizer. When the beam's intensity is measured by a power meter behind the CD, optical integration over

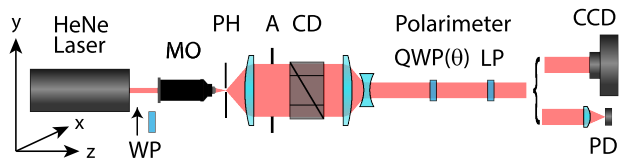


Fig. 3. Experimental setup: Helium–neon laser followed by an optional wave plate (WP), a spatial filter comprised of a microscope objective (MO) and pinhole (PH), variable iris aperture (A), Cornu depolarizer (CD), a polarimeter consisting of a rotatable quarter-wave plate (QWP, angle θ with respect to the LP) and linear polarizer (LP). A CCD camera acquires spatially resolved polarization properties and is replaced by a Si photodetector for spatially integrated polarization measurements.

the illuminated detector surface is considered by integrating elements of the matrix in Eq. (2) using polar coordinates (ρ, θ) as follows [25]:

$$\langle \cos(\phi) \rangle_{\rho, \theta} = \frac{1}{\pi} \int_0^{2\pi} \int_0^1 \cos[\phi \cdot \rho \cdot \cos(\theta)] d\rho d\theta = 2 \frac{J_1(\phi)}{\phi}, \quad (3)$$

$$\langle \sin(\phi) \rangle_{\rho, \theta} = \frac{1}{\pi} \int_0^{2\pi} \int_0^1 \sin[\phi \cdot \rho \cdot \sin(\theta)] d\rho d\theta = 0, \quad (4)$$

where J_1 is a first-order Bessel function of the first kind. In these calculations, a beam profile with uniform irradiance was assumed, which is adequate considering that the Cornu depolarizer's center was aligned with the beam's center. By integration of the matrix M_{Cornu} in Eq. (2) as performed in Eqs. (3) and (4), the off-axis elements vanish, yielding a spatially averaged matrix $\langle M_{\text{Cornu}} \rangle$. By multiplying this matrix with a linearly polarized input Stokes vector, light that is collected behind the Cornu depolarizer now has the following degree of polarization (DOP):

$$\text{DOP} = \frac{\sqrt{S_1^2 + S_2^2 + S_3^2}}{S_0} = 2 \left| \frac{J_1(\phi)}{\phi} \right|. \quad (5)$$

This result shows that the DOP can be tuned via the phase ϕ , which will be used in the following for the generation of spatially unpolarized light (DOP = 0).

3. EXPERIMENTAL SETUP AND METHODS

A. Setup

Our experimental setup is depicted in Fig. 3 in more detail. A helium–neon laser emits linearly polarized light (99% DOP), while operating at a wavelength of 632.8 nm with a continuous optical output power of 11 mW and a $1/e^2$ beam diameter of 0.65 mm. The laser's polarization axis is oriented in parallel to the y -axis, as shown in Fig. 3. The laser's beam profile consists of a TEM₀₀ fundamental mode with spatial noise present due to intensity fluctuations as a result of scattering. To mitigate noise, a spatial mode filter is realized by placing a microscope objective (10× magnification, NA = 0.85) and a pinhole aperture (30 μm diameter) into the beam path to produce a smooth Gaussian beam profile by suppressing residual transverse modes and spatial noise [61]. The pinhole diameter d was chosen according to the following formula [62]:

$$d = 1.5 \cdot 1.27 \frac{\lambda f}{D}, \quad (6)$$

with the spot size D of the beam entering the microscope objective, laser wavelength λ , and microscope objective's focal length f . The microscope objective was chosen such that the cone of light behind the pinhole is collected entirely by a subsequent lens, maintaining a Gaussian intensity distribution of the beam throughout the setup. A plano-convex lens ($f = 400$ mm) with a sufficiently clear aperture behind the spatial filter collimates the entire beam. This lens in combination with the spatial filter now acts as a Keplerian telescope, which serves to expand the laser beam up to 50 mm in diameter. A variable iris aperture A placed behind this telescope clips the beam to a desired width. The Cornu depolarizer is exploited to spatially depolarize the input beam. Our setup is complemented by a Galilean telescope consisting of another identical plano-convex lens ($f = 400$ mm) and a bi-concave lens ($f = -75$ mm), which tapers the beam diameter for the subsequently following detection analysis. Finally, the polarization of the transmitted light is examined by an imaging polarimeter consisting of a rotatable quarter-wave plate followed by a linear polarizer, which gives access to the Stokes parameters for both the spatially resolved and spatially integrated detection.

B. Methods

1. Spatially Resolved and Spatially Integrated Stokes Parameters

In the following sections, the depolarization of various input polarization states is investigated. We modify the input polarization state of light by inserting a wave plate right behind the laser and rotating its fast axis with respect to the laser's polarization axis. The Stokes parameters of the output beams are obtained using a Schaefer–Collett polarimeter and measuring the spatially integrated beam intensity with a power meter or a CCD in the spatially resolved case. While the linear polarizer's transmission axis remains fixed, a quarter-wave plate (rotation angle θ) is rotated in 10° increments, and the beam intensity is measured for every fixed position of the quarter-wave plate. The normalized Stokes parameters s_1 , s_2 , and s_3 are derived by conducting a Fourier series analysis [54,58].

For further inspection of the polarization states, spatially resolved Stokes parameter distributions of the beam are recorded by a CCD camera (WinCamD-UCM) positioned behind the Schaefer–Collett polarimeter. The surface area of the CCD sensor is approximately 8.6 mm \times 6.9 mm and has a resolution of 1.2 megapixels. Before measuring polarization parameters, the plano-convex lens is adjusted to a position such that the incident beam is collimated and fills the imaged area. After the intensity distribution is measured, Stokes parameter analysis is performed individually for every pixel again by Fourier series calculations [58]. The spatial Stokes parameters $s_1(x, y)$, $s_2(x, y)$, $s_3(x, y)$, and DOP(x, y) are then normalized and plotted as a function of the spatial variables x and y . For measurements of polarization parameters profiles, the iris aperture in Fig. 3 is fully opened to its largest diameter of 50 mm.

2. Degree of Polarization

The degree of polarization depending on the illuminated cross-section of the output light exiting the Cornu depolarizer is measured by varying the iris aperture diameter prior to the Cornu depolarizer. First, the iris diameter is reduced to a lowest setting of 2 mm and a Stokes parameter analysis is performed for this configuration. In a next step, the aperture is opened further in 2 mm successive increments, and for every step, the Stokes parameter analysis is repeated. The evaluated Stokes parameters and DOP are plotted as a function of aperture diameter.

4. RESULTS

First, we verify the imaging quality of our set-up without the CD. Then, we insert the CD and a subsequent polarizer, set the aperture opening to 50 mm, and observe a horizontal polarization fringe pattern on a screen behind the polarizer. We then trace the beam by moving the screen away from the CD to check for any immediately visible longitudinal effects. The only visible longitudinal effect that arises is a certain, small degree of barrel distortion, which is shown in the following results for all three input polarization states. In this section, Stokes parameters of the beam transmitted through the Cornu depolarizer and corresponding degrees of polarization of the output light are presented for three distinct input polarization states: linearly y -polarized, linearly x -polarized, and circularly polarized. We choose these states as a benchmark of the Cornu depolarizer’s performance. The spatially resolved measurements for each input polarization state are complemented by their respective measurements of the degree of polarization for a range of aperture diameters. This set of measurements fully characterizes the Cornu depolarizer and validates its expected depolarization functionality.

A. Linearly y -Polarized Input

1. Spatially Resolved and Spatially Integrated Stokes Parameters

For linearly y -polarized input light incident upon the Cornu depolarizer with a polarization axis parallel to the y -axis, the output beam that exits the Schaefer–Collett polarimeter shown in Fig. 3 exhibits polarization parameters as depicted in Fig. 4. Since the camera was not positioned precisely in the center of the beam, the polarization distributions are labeled with a separate coordinate system indicating the (x, y) -pixel position on the CCD sensor. The spatial distribution of $s_1(x, y)$ is dominated by equidistant polarization fringes of alternating values across the y -axis of the beam ranging between values of -1 and 1 , which suggest that the orientation of input linear polarization is periodically dispersed by the Cornu depolarizer. The beam intensity remains constant across the x -axis and displays only a slight barrel distortion around the beam’s edge. Clipping the beam in front of the CD to various widths using the iris aperture does not affect this pattern qualitatively, which implies that the fringe width depends only on the geometry and material of the Cornu depolarizer. The modulation across the depolarizer’s y -axis is examined by extracting values of $s_1(x, y)$ along

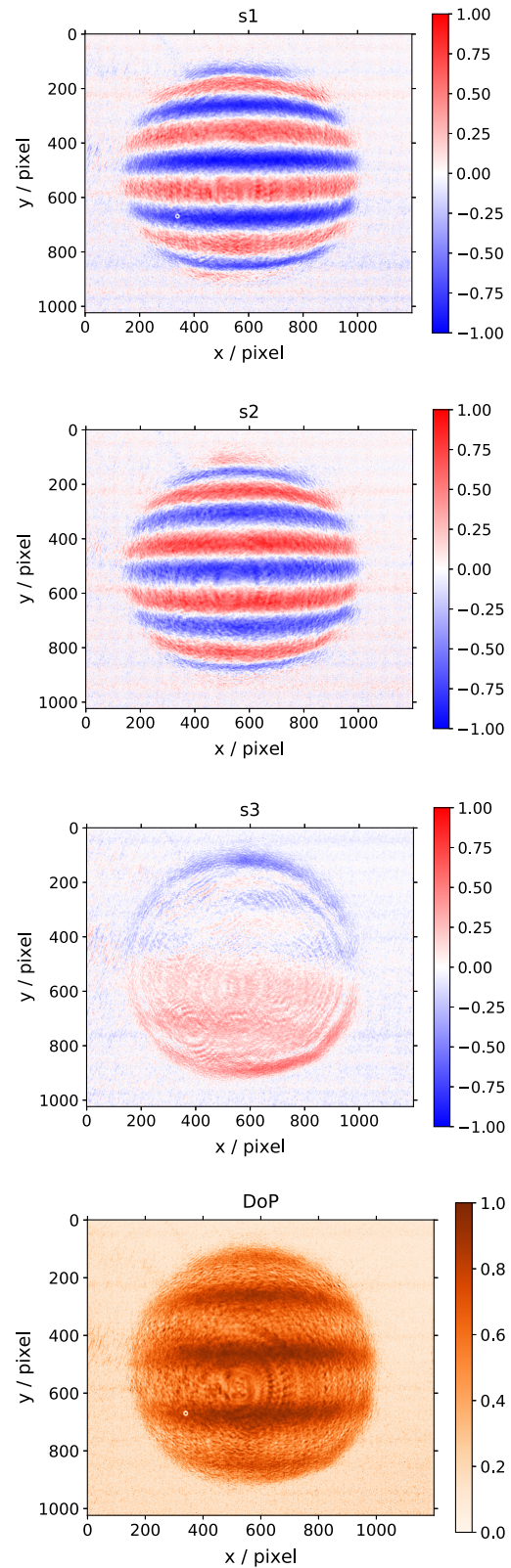


Fig. 4. CCD images illustrating the spatial distribution of normalized Stokes parameters $s_1(x, y)$, $s_2(x, y)$, and $s_3(x, y)$ for linearly y -polarized input light. Red colors indicate positive values, whereas blue indicate negative values. A small degree of barrel distortion is visible around the profile’s edge.

a central symmetry axis of the beam. The fringe width η can be interpreted as a 180° (or π) rotation of the polarization axis about the beam's propagation axis and is calculated using the specific optical rotary power ρ_R and the wedge cut angle α :

$$\eta = \frac{\pi}{\rho_R \tan(\alpha)} = \frac{\pi}{\frac{2\pi}{\lambda}(n_l - n_r) \tan(\alpha)} = 8.34 \text{ mm.} \quad (7)$$

This width is in agreement with six fringes observed and corresponds to full illumination of the Cornu depolarizer's front facet: $6\eta \approx 50$ mm. Using these calculations of the fringe width and the front facet height of the depolarizer, the spot size of the beam shown in the CCD data can be estimated. A similar fringe pattern emerges for the spatial distribution of the Stokes parameter $s_2(x, y)$, although the entire pattern is shifted along the y -axis by $\pi/2$. Comparable patterns are observed for a simulation of the fringe patterns that can be seen in Fig. 5 for the spatial distribution of the Stokes parameters $s_1(x, y)$ and $s_2(x, y)$. The shift of all Stokes parameter values between the two distributions $s_1(x, y)$ and $s_2(x, y)$ by $\pi/2$ is also clearly shown in this simulation. As expected, a considerably smaller, nearly zero modulation occurs for the Stokes parameter $s_3(x, y)$, confirming that only linear polarization components are mixed by the Cornu depolarizer. The upper half of the distribution of $s_3(x, y)$ in Fig. 4 exhibits slightly higher overall negative values for $s_3(x, y)$, while the lower half displays slightly lower overall positive values for $s_3(x, y)$, which is due to an insufficient phase dispersion for the s_3 components of light. In this particular distribution, weak, concentric circular fringes are visible, which result from clipping the beam slightly at the first two relevant aperture stops (the plano-convex lens and the subsequent iris aperture). The spatial distribution of DOP values in the bottom of Fig. 4 also has visible fringes corresponding to the red fringes shown in the distribution of $s_1(x, y)$. A faint spiral feature in the beam's center results from deficiencies of the quarter-wave plate of the Schaefer–Collett polarimeter. For all four spatially resolved polarization distributions, a small degree of spatial barrel distortion is visible toward the edges of the beam profiles, which is due to a non-ideal positioning of the collimating lenses behind the CD. The nonuniform distribution of $\text{DOP}(x, y)$ is

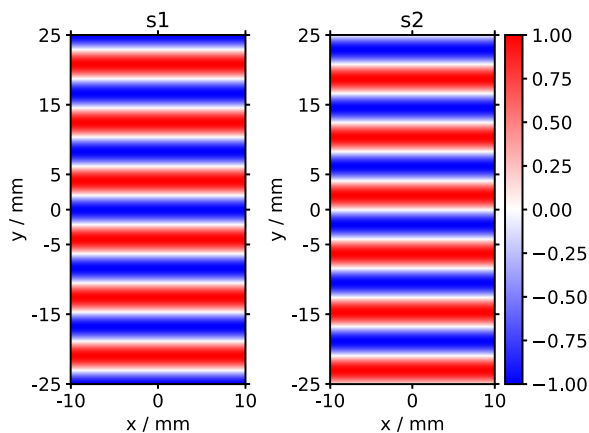


Fig. 5. Simulated polarization fringes of the Stokes parameters for y -polarized incident light. The Stokes parameter distribution $s_3(x, y)$ is not displayed here as the image would appear totally white since the values of $s_3(x, y)$ are zero overall.

due to errors resulting from slight off-axis misalignment of the CD with respect to the beam's propagation axis.

2. Degree of Polarization

The evolution of the Stokes parameter s_1 and DOP as shown in Fig. 6 for increasing values of aperture-determined input diameters is reminiscent of Bessel functions of the first kind. A similar behavior has been derived theoretically for Mueller matrix elements of a dual Babinet compensator [25] and was described to some degree for single-wedge [42] and double-wedge depolarizers in numerical simulations [44].

For the DOP curve depicted in Fig. 6, a first-order Bessel function of the first kind J_1 is plotted by inserting Eq. (1) into Eq. (5) and substituting the Cornu depolarizer's length L by the relation $L = h \tan(\alpha)$, where h denotes the aperture diameter:

$$\text{DOP}(h) = 2 \left| \frac{J_1 \left[\frac{2\pi}{\lambda} (n_l - n_r) h \tan(\alpha) \right]}{\frac{2\pi}{\lambda} (n_l - n_r) h \tan(\alpha)} \right|. \quad (8)$$

The simulation of the DOP is indicated in Fig. 6 by a continuous red line. As can be seen in Fig. 6, for certain aperture diameters, where the curve of s_1 intersects with the x -axis, the DOP drops to minimum values of 8% for an aperture diameter of 10 mm and to 5% for a aperture diameter of 20 mm, indicating that the output light is almost completely spatially unpolarized. For all other aperture diameters, the residual polarization is comprised of a linear superposition of non-zero values of the s_1 and s_2 parameters. As anticipated, s_3 remains at a very low value (below 5%) for all aperture diameters.

B. Linearly x-Polarized Input

1. Spatially Resolved and Spatially Integrated Stokes Parameters

In a second experiment, a half-wave plate was inserted in front of the CD and rotated to an angle of 45° with respect to the laser's polarization axis, generating linearly x -polarized light and the same measurement series were carried out for all Stokes parameters and DOP. As shown in Fig. 7, similar spatial polarization distributions are observed for $s_1(x, y)$, $s_2(x, y)$, and $s_3(x, y)$ compared to Fig. 4. For the polarization parameters

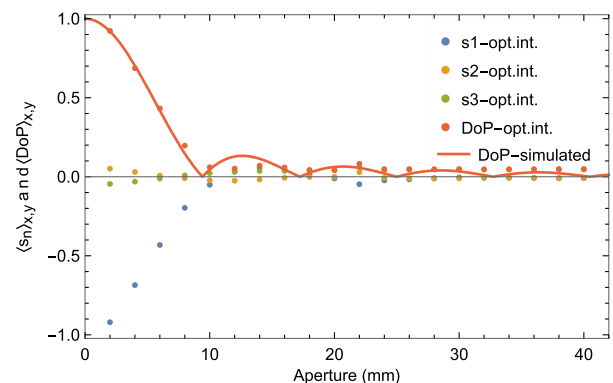


Fig. 6. Spatially integrated Stokes parameters s_1 , s_2 , and s_3 and DOP as a function of iris diameter for linearly y -polarized input light. The red dots indicate experimental data of the DOP, and the full line represents a simulation of the DOP according to Eq. (5).

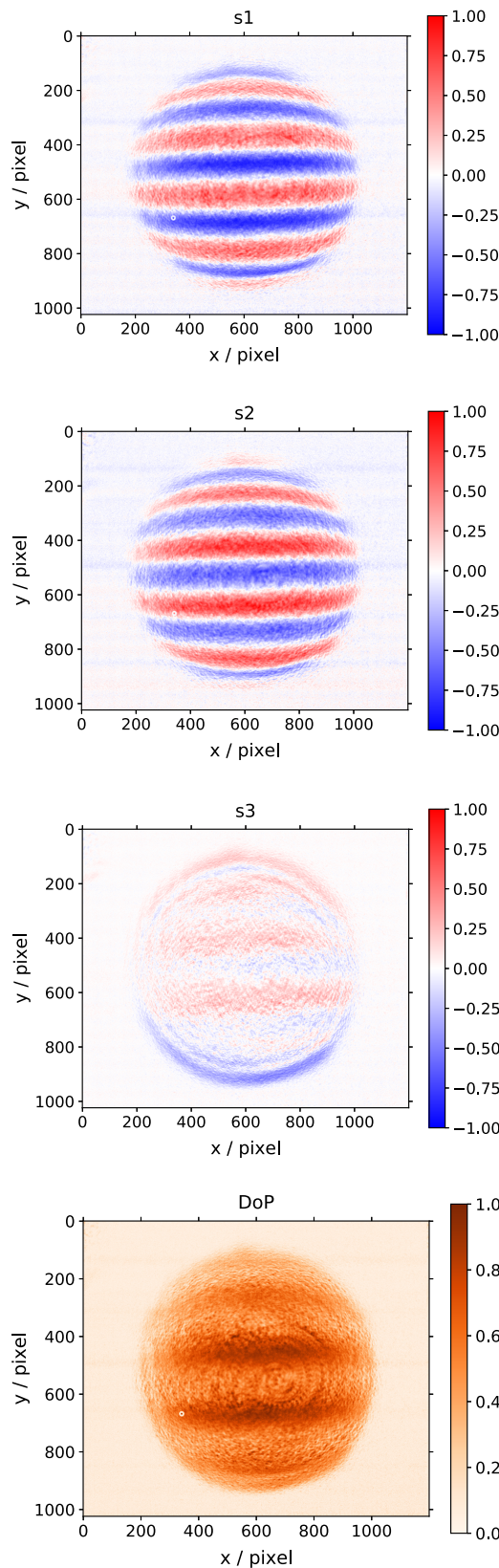


Fig. 7. CCD images illustrating the spatial distribution of the normalized Stokes parameters $s_1(x, y)$, $s_2(x, y)$, and $s_3(x, y)$ for linearly x -polarized input light. Red colors indicate positive values, whereas blue indicate negative values. A small degree of barrel distortion is visible around the profile's edge.

$s_1(x, y)$ and $s_2(x, y)$, the same sinusoidal modulation along the y -axis is present. However, compared to the previous case with linearly y -polarized light, in both cases, the fringe position is shifted by a half period of the fringe width η along the y -axis for $s_1(x, y)$ and $s_2(x, y)$. For the polarization parameter $s_3(x, y)$, a similar distribution was measured compared to the one for $s_3(x, y)$ in Fig. 4, while for the DOP the fringes are still present. Considering the data obtained for this input polarization as shown in Fig. 7, it is evident that the depolarization effect is independent of the input polarization angle. This is also somewhat apparent when examining the matrix elements in Eq. (2).

2. Degree of Polarization

For linearly x -polarized input light, the Stokes parameters and DOP were measured and are shown in Fig. 8. For increasing aperture diameters, it is now the evolution of s_1 that follows the experimental DOP results and that nicely coincides with the simulated DOP results. Here, for small aperture values, the contributions of s_2 and s_3 to DOP are slightly higher compared to Fig. 6, and both s_2 and s_3 drop $<10\%$ for apertures >10 mm. Again, low DOP values of 8% and 5% were achieved for 20 mm and 30 mm, respectively. The comparatively higher values of s_2 and s_3 for aperture diameters between 2 mm and 10 mm are likely the result of diattenuation and the non-ideal retardance of the half-wave plate (HWP) that is used to generate linearly x -polarized input light, resulting in additional, residual elliptical components of the input light [63].

C. Circularly Polarized Input

1. Spatially Resolved and Spatially Integrated Stokes Parameters

By placing a quarter-wave plate in front of the CD shown in Fig. 3 and rotating it to a 45° angle with respect to the laser's polarization axis, circularly polarized light is produced, which then enters the Cornu depolarizer. The output Stokes parameters can be seen in Fig. 9. Again, Stokes parameter analysis is performed for the full opening of the beam (50 mm), revealing spatial polarization distributions. In the resulting distributions,

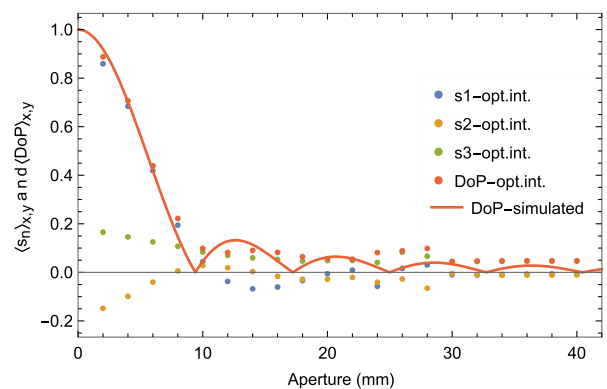


Fig. 8. Spatially integrated Stokes parameters s_1 , s_2 , and s_3 and DOP as a function of aperture diameter for linearly x -polarized input light. A simulated function of the DOP as generated by using Eq. (5) is represented by the continuous red line.

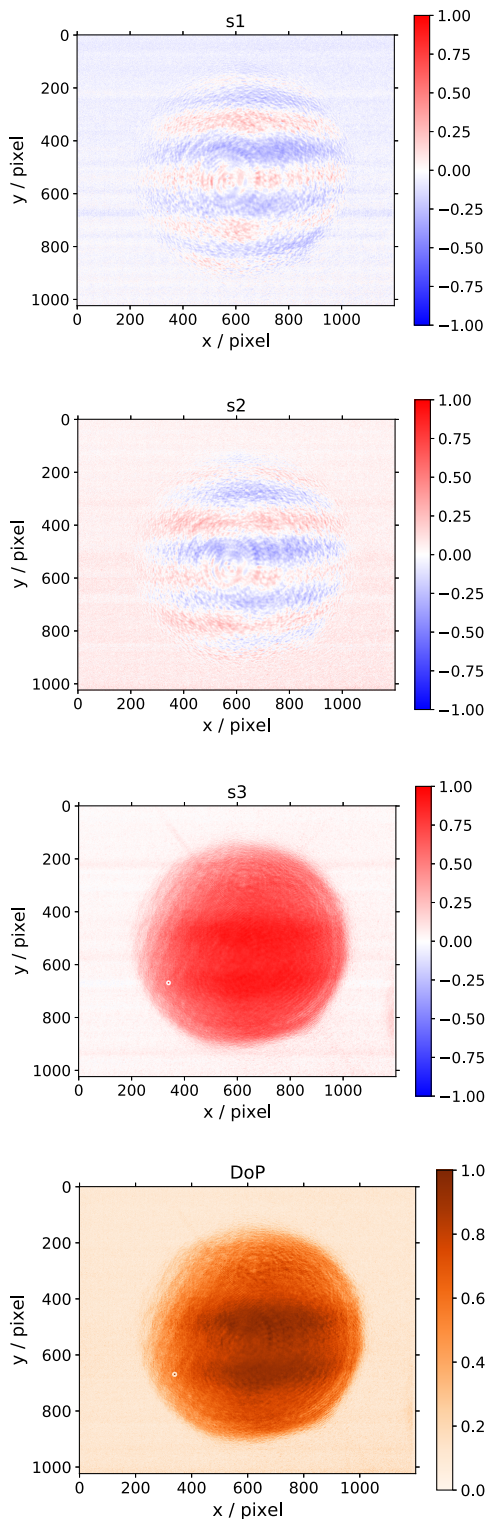


Fig. 9. CCD images illustrating the spatial distribution of the normalized Stokes parameters $s_1(x, y)$, $s_2(x, y)$, and $s_3(x, y)$ for circularly polarized input light. Red colors indicate positive values, whereas blue indicate negative values. A small degree of barrel distortion is visible around the profile's edge.

a fringe pattern is still faintly visible for the Stokes parameters $s_1(x, y)$ and $s_2(x, y)$; however, the contrast between the fringes is notably diminished. Comparing the distribution of

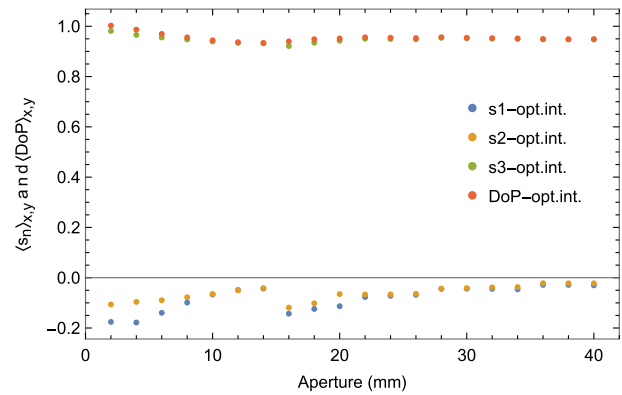


Fig. 10. Spatially integrated Stokes parameters s_1 , s_2 , and s_3 and DOP as a function of aperture diameter for circularly polarized input.

$s_1(x, y)$ to its corresponding one in Fig. 4, the entire pattern is shifted along the y -axis by $\pi/2$. For the polarization parameter $s_3(x, y)$, high values are predominant across the beam's profile without any visible polarization fringes. This confirms that the Cornu depolarizer has almost no influence on circularly polarized components of input light.

2. Degree of Polarization

For circularly polarized input, the DOP was measured using the same procedure as for linearly polarized input. The results can be seen in Fig. 10. In this case, the DOP exhibits mostly constant, high values above 0.94 for all aperture diameters in conjunction with a high s_3 value above 0.92. This confirms yet again that the Cornu depolarizer has nearly no influence on circularly polarized components. The non-ideal retardation and diattenuation of the quarter-wave plate placed in front of the CD in Fig. 3 is a probable cause for the s_3 values not being closer to a value of 1. The imperfections of the wave-plate introduce residual elliptical components [63], leading to comparatively lower values of s_1 and s_2 in this case. A similar effect was also observed for the spatially integrated DOP of x -polarized input.

D. DISCUSSION

The lowest DOP values were achieved for a small aperture diameter of roughly 10 mm. Increasing the aperture diameter further only increases the potential for errors due to off-axis effects playing a larger role. Thus, the aperture diameter range up to the first DOP minimum is a desirable optimal working range for most applications of the Cornu depolarizer. This is a factor that should be taken into account when constructing a Cornu depolarizer. The results presented here offer a deeper insight into the Cornu depolarizer's action for a monochromatic source of light. The spatially resolved measurements are consolidated by spatially integrated measurements for every input polarization state. The measured CCD images provide a convincing overall survey of output polarization states produced for certain input polarization states. In particular, the spatially integrated results for various aperture diameters could be reproduced to a high degree, coinciding with theoretical calculations based on a description of a Cornu depolarizer given by McGuire *et al.* [25].

The noticeable polarization fringes were explained analytically by taking into account the induced spatial phase shifts for simulations of the degree of polarization, in good agreement with the experimental data. A qualitative change of the fringes position and their absence for certain input polarizations could be explained within the Mueller calculus framework. Apart from this, our findings indicate that we achieved the generation of an extreme case of type II unpolarized light, namely “phase averaged equatorial-coherent states” [9] in close approximation for certain aperture diameters with minimal DOP values of spatially integrated measurements.

From the point of view of the Poincaré sphere, the output polarization generated here is equivalent to a distribution of polarization states that are evenly spread across the sphere’s equator, as illustrated by red dots in Fig. 1. Since this distribution is symmetrical with respect to the sphere’s origin, with contributions of $s_1(x, y)$ and $s_2(x, y)$ being on par, the polarization state manifests itself as unpolarized. This polarization state is somewhat similar to temporally unpolarized light [15] generated by the emission of two independent lasers with orthogonal polarization states in superposition [8,11].

Further investigation of this type of spatially unpolarized light will focus on its polarization correlation properties in the context of ghost polarimetry [47]. The feature of an easily tunable DOP as we have demonstrated by exploiting the Cornu depolarizer could be the basis for further measurements, notably polarization correlations between type I unpolarized light [15] and type II spatially depolarized light, and in particular in the recently emerging field of Floquet engineering [64,65].

5. CONCLUSION

In this work, the polarization properties of an optically active Cornu depolarizer were characterized extensively using Stokes parameter analysis. The spatial distributions of the output beam’s Stokes parameters were presented for input light that was either linearly or circularly polarized. The distinctive polarization fringe patterns of the spatial Stokes parameters and corresponding degree of polarization were quantified using Stokes formalism in conjunction with Mueller matrix calculus, displaying consistent agreement between theoretical analysis and experimental data. For certain aperture-determined input diameters of linearly polarized light, very low DOP values of 5% were achieved, which demonstrates the Cornu depolarizer’s potential to produce spatially randomly unpolarized light of high fidelity for an arbitrary orientation of the input polarization axis. Considering the circular birefringence of quartz, this can be done seamlessly across a wide wavelength range from the UV to near-IR [66]. Polychromatic input light can also be accommodated, since dispersion adds positively to the polarization scrambling. Furthermore, partially polarized light is accessible by simply tuning the aperture diameter. Since intensity statistics, spatial correlations, and noise levels are preserved, this robust depolarization scheme is advantageous for certain scenarios compared to other methods that rely on temporal depolarization such as pseudo-thermal light sources [67] (scattering by rotating diffuser discs) or rotating wave-plates [58]. The birefringent trait present in a variety of crystalline materials

provides flexibility with regard to parameters such as optical rotary power [48].

In conclusion, these findings demonstrate that the Cornu depolarizer remains an indispensable tool for the controlled generation of unpolarized light. This characterization of the Cornu depolarizer reconciliated theoretical predictions with experimental data and serves as guidance for the design and selection of appropriate parameters of a Cornu depolarizer for future applications.

Funding. Deutscher Akademischer Austauschdienst (Breakthroughs in Ghost Imaging); Deutsche Forschungsgemeinschaft (EL 105-21).

Acknowledgment. The authors thank Andreas Herdt for fruitful and stimulating discussions and experimental support and Th. Führer for the loan of a CCD camera. We gratefully acknowledge discussions on the CD with Dr. Götz Zinner from B. Halle Nachfl. GmbH (Berlin) and the competent and innovative craftsmanship of this extraordinary optical manufacture. We thank Prof. A. T. Friberg for stimulating discussions about polarization and for two wonderful conferences on coherence and polarization.

Disclosures. The authors declare no conflicts of interest.

Data Availability. Data underlying the results presented in this paper are not publicly available at this time but may be obtained from the authors upon reasonable request.

REFERENCES

1. A. Goldberg, P. de la Hoz, G. Björk, A. Klimov, M. Grassl, G. Leuchs, and L. Sanchez-Soto, “Quantum concepts in optical polarization,” *Adv. Opt. Photon.* **13**, 1–73 (2020).
2. R. T. Birge, “On the nature of unpolarized light,” *J. Opt. Soc. Am.* **25**, 179–182 (1935).
3. H. Hurwitz, “The statistical properties of unpolarized light,” *J. Opt. Soc. Am.* **35**, 525–531 (1945).
4. E. Verdet, “Étude sur la constitution de la lumière non polarisée et de la lumière partiellement polarisée,” *Annales Scientifiques de l’École Normale Supérieure* **2**, 291–316 (1865).
5. B. Lyot, “Recherches sur la polarisation de la lumière des planètes et de quelques substances terrestres,” *Ann. l’Observatoire Astron. Phys. Paris (Meudon)* **8**, 100–104 (1928).
6. H. Paul and J. Wegmann, “Polarization correlations in unpolarized light,” *Opt. Commun.* **112**, 85–90 (1994).
7. J. Lehner, U. Leonhardt, and H. Paul, “Unpolarized light: Classical and quantum states,” *Phys. Rev. A* **53**, 2727–2735 (1996).
8. J. Lehner, H. Paul, and G. Agarwal, “Generation and physical properties of a new form of unpolarized light,” *Opt. Commun.* **139**, 262–269 (1997).
9. A. Luis, “Degree of polarization of type-II unpolarized light,” *Phys. Rev. A* **75**, 053806 (2007).
10. T. Setälä, A. Shevchenko, M. Kaivola, and A. T. Friberg, “Polarization time and length for random optical beams,” *Phys. Rev. A* **78**, 033817 (2008).
11. A. Shevchenko, M. Roussey, A. T. Friberg, and T. Setälä, “Polarization time of unpolarized light,” *Optica* **4**, 64–70 (2017).
12. A. Shevchenko and T. Setälä, “Interference and polarization beating of independent arbitrarily polarized polychromatic optical waves,” *Phys. Rev. A* **100**, 023842 (2019).
13. M. Roskopf, T. Mohr, and W. Elsässer, “Ghost polarization communication,” *Phys. Rev. Appl.* **13**, 034062 (2020).
14. A. Hannonen, B. J. Hoenders, W. Elsässer, A. T. Friberg, and T. Setälä, “Ghost polarimetry using stokes correlations,” *J. Opt. Soc. Am. A* **37**, 714–719 (2020).
15. F. Kroh, M. Roskopf, and W. Elsässer, “Ultra-fast stokes parameter correlations of true unpolarized thermal light: type-I unpolarized light,” *Opt. Lett.* **45**, 5840–5843 (2020).
16. K. Bohm, K. Petermann, and E. Weidel, “Performance of Lyot depolarizers with birefringent single-mode fibers,” *J. Lightwave Technol.* **1**, 71–74 (1983).

17. K. Mochizuki, "Degree of polarization in jointed fibers: the Lyot depolarizer," *Appl. Opt.* **23**, 3284–3288 (1984).
18. V. Mazurczyk and J. Zyskind, "Polarization dependent gain in erbium doped-fiber amplifiers," *IEEE Photon. Technol. Lett.* **6**, 616–618 (1994).
19. A. Shaham and H. S. Eisenberg, "Realizing controllable depolarization in photonic quantum-information channels," *Phys. Rev. A* **83**, 022303 (2011).
20. A. Shaham and H. S. Eisenberg, "Realizing a variable isotropic depolarizer," *Opt. Lett.* **37**, 2643–2645 (2012).
21. Á. Rivas and A. Luis, "SU(2)-invariant depolarization of quantum states of light," *Phys. Rev. A* **88**, 052120 (2013).
22. K. Perlicki, "Investigation of the state of polarization distribution generated by polarization scramblers on the Poincaré sphere," *Opt. Commun.* **252**, 58–63 (2005).
23. E. Waluschka, M. Wilson, M. Quijada, B. McAndrew, and L. Ding, "ORCA's depolarizer," *Proc. SPIE* **8153**, 81530U (2011).
24. G. Ropars, G. Gorre, A. L. Floch, J. Enoch, and V. Lakshminarayanan, "A depolarizer as a possible precise sunstone for viking navigation by polarized skylight," *Proc. R. Soc. A* **468**, 671–684 (2011).
25. J. P. McGuire and R. A. Chipman, "Analysis of spatial pseudodepolarizers in imaging systems," *Proc. SPIE* **1166**, 95–108 (1990).
26. C. Chou, W.-C. Kuo, and C.-Y. Han, "Circularly polarized optical heterodyne interferometer for optical activity measurement of a quartz crystal," *Appl. Opt.* **42**, 5096–5100 (2003).
27. O. Arteaga, A. Canillas, and G. E. Jellison, "Determination of the components of the gyration tensor of quartz by oblique incidence transmission two-modulator generalized ellipsometry," *Appl. Opt.* **48**, 5307–5317 (2009).
28. C. Samlan and N. K. Viswanathan, "Generation of vector beams using a double-wedge depolarizer: Non-quantum entanglement," *Opt. Laser Eng.* **82**, 135–140 (2016).
29. G. M. Lerman, L. Stern, and U. Levy, "Generation and tight focusing of hybridly polarized vector beams," *Opt. Express* **18**, 27650–27657 (2010).
30. O. Arteaga, E. Garcia-Caurel, and R. Ossikovski, "Stern-Gerlach experiment with light: separating photons by spin with the method of a Fresnel," *Opt. Express* **27**, 4758–4768 (2019).
31. A. M. Beckley, T. G. Brown, and M. A. Alonso, "Full Poincaré beams," *Opt. Express* **18**, 10777–10785 (2010).
32. C. Alpmann, C. Schlickriede, E. Otte, and C. Denz, "Dynamic modulation of Poincaré beams," *Sci. Rep.* **7**, 8076 (2017).
33. G. Piquero, L. Monroy, M. Santarsiero, M. Alonzo, and J. C. G. de Sande, "Synthesis of full Poincaré beams by means of uniaxial crystals," *J. Opt.* **20**, 065602 (2018).
34. G. Piquero, R. Martnez-Herrero, J. C. G. de Sande, and M. Santarsiero, "Synthesis and characterization of non-uniformly totally polarized light beams: tutorial," *J. Opt. Soc. Am. A* **37**, 591–605 (2020).
35. J. Ellis and A. Dogariu, "Differentiation of globally unpolarized complex random fields," *J. Opt. Soc. Am. A* **21**, 988–993 (2004).
36. J. Ellis and A. Dogariu, "Discrimination of globally unpolarized fields through stokes vector element correlations," *J. Opt. Soc. Am. A* **22**, 491–496 (2005).
37. B.-Y. Wei, P. Chen, S.-J. Ge, L.-C. Zhang, W. Hu, and Y.-Q. Lu, "Liquid crystal depolarizer based on photoalignment technology," *Photon. Res.* **4**, 70–73 (2016).
38. Y. Wang, W. Zhu, C. Zhang, Q. Fan, L. Chen, H. Lezec, A. Agrawal, and T. Xu, "Ultra-compact visible light depolarizer based on dielectric metasurface," *Appl. Phys. Lett.* **116**, 051103 (2020).
39. R. Ossikovski, M. Anastasiadou, S. B. Hatit, E. Garcia-Caurel, and A. D. Martino, "Depolarizing Mueller matrices: how to decompose them?" *Phys. Status Solidi A* **205**, 720–727 (2008).
40. R. Ossikovski, "Canonical forms of depolarizing Mueller matrices," *J. Opt. Soc. Am. A* **27**, 123–130 (2009).
41. J. J. Gil, "Structure of polarimetric purity of a Mueller matrix and sources of depolarization," *Opt. Commun.* **368**, 165–173 (2016).
42. J. H. Ge, Z. Chen, Y. F. Chen, C. Y. Chen, Y. F. Zhai, J. Zhang, Z. Sui, H. H. Lin, J. J. Wang, and Q. H. Deng, "Optimized design of parameters for wedge-crystal depolarizer," *Appl. Mech. Mater.* **110**–116, 3351–3357 (2011).
43. M. Griot, *Optics Guide 4* (1988).
44. Y. Liu and G. Li, "Compound quartz depolarizer," *Optoelectron. Adv. Mater. Rapid Commun.* **2**, 178–180 (2008).
45. Y. Jin and W. Shen, "Design of double wedge depolarizer for grating imaging spectrometer," *Proc. SPIE* **10255**, 1025522 (2017).
46. J. C. G. de Sande, M. Santarsiero, G. Piquero, and F. Gori, "Longitudinal polarization periodicity of unpolarized light passing through a double wedge depolarizer," *Opt. Express* **20**, 27348–27360 (2012).
47. H. Partanen, A. T. Friberg, T. Setälä, and J. Turunen, "Spectral measurement of coherence stokes parameters of random broadband light beams," *Photon. Res.* **7**, 669–677 (2019).
48. V. A. Bagan, B. L. Davydov, and I. E. Samartsev, "Characteristics of cornu depolarisers made from quartz and paratellurite optically active crystals," *Quantum Electron.* **39**, 73–78 (2009).
49. E. Collett, *Field Guide to Polarization* (SPIE, 2005), Vol. **FG05**.
50. B. H. Billings, "A monochromatic depolarizer," *J. Opt. Soc. Am.* **41**, 966–975 (1951).
51. L. Bergmann and C. Schaefer, *Lehrbuch der Experimentalphysik* (Walter de Gruyter, 1978).
52. A. Cornu, "De la réfraction à travers un prisme suivant une loi quelconque," *Annales Scientifiques de l'École Normale Supérieure* **3**, 1–46 (1874).
53. A. Cornu, "Détermination des trois paramètres optiques principaux d'un cristal, en grandeur et en direction, par le réfractomètre," *Bulletin de la Société Française de Minéralogie* **25**, 7–15 (1902).
54. B. Schaefer, E. Collett, R. Smyth, D. Barrett, and B. Fraher, "Measuring the stokes polarization parameters," *Am. J. Phys.* **75**, 163–168 (2007).
55. H. G. Berry, G. Gabrielse, and A. E. Livingston, "Measurement of the stokes parameters of light," *Appl. Opt.* **16**, 3200–3205 (1977).
56. G. H. Stokes, "On the composition and resolution of streams of polarized light from different sources," *Trans. Camb. Philos. Soc.* **9**, 399–416 (1852) [Reprinted in *Mathematical and Physical Papers* by Cambridge University Press (2009)].
57. C. Brosseau, *Fundamentals of Polarized Light: A Statistical Optics Approach* (Wiley, 1998).
58. E. Collett, *Polarized Light: Fundamentals and Applications* (Marcel Dekker, 1993).
59. J. Ellis and A. Dogariu, "Optical polarimetry of random fields," *Phys. Rev. Lett.* **95**, 203905 (2005).
60. A. Yariv and P. Yeh, *Optical Waves in Crystals: Propagation and Control of Laser Radiation*, Wiley Classics Library (Wiley, 2003).
61. A. K. Sharma, R. K. Patidar, D. Daiya, A. Joshi, P. A. Naik, and P. D. Gupta, "Simple and sensitive technique for alignment of the pinhole of a spatial filter of a high-energy, high-power laser system," *Appl. Opt.* **52**, 2546–2554 (2013).
62. J. Pinnell, A. Klug, and A. Forbes, "Spatial filtering of structured light," *Am. J. Phys.* **88**, 1123–1131 (2020).
63. M. Bass, C. DeCusatis, J. Enoch, V. Lakshminarayanan, G. Li, C. MacDonald, V. Mahajan, and E. Van Stryland, *Handbook of Optics, Third Edition Volume II: Design, Fabrication and Testing, Sources and Detectors, Radiometry and Photometry*, 3rd ed. (McGraw-Hill, 2009).
64. V. L. Quito and R. Flint, "Polarization as a tuning parameter for Floquet engineering: Magnetism in the honeycomb, square, and triangular Mott insulators," *Phys. Rev. B* **103**, 134435 (2021).
65. V. L. Quito and R. Flint, "Floquet engineering correlated materials with unpolarized light," *Phys. Rev. Lett.* **126**, 177201 (2021).
66. G. Ghosh, "Dispersion-equation coefficients for the refractive index and birefringence of calcite and quartz crystals," *Opt. Commun.* **163**, 95–102 (1999).
67. W. Martienssen and E. Spiller, "Coherence and fluctuations in light beams," *Am. J. Phys.* **32**, 919–926 (1964).